# Steering Magnetic Particles by an Array of Rotatable Permanent Magnets: Control Design and Experimental Verification

Janaka Madhusankha, Lahiru Ekanayake, and Arash Komaee

Abstract—This paper presents experimental results to verify a novel concept of magnetic manipulation in which arrays of permanent magnets and electromechanical actuators generate and effectively control magnetic fields, through which, magnetic objects can be manipulated from a distance without any direct contact. This concept is realized by an experimental setup that consists of six diametrically magnetized permanent magnets actuated by rotary servomotors to control their directions, by which, the aggregate magnetic field is controlled in a planar circular workspace. To leverage this magnetic field for control of magnetic objects inside the workspace, a feedback loop must be established to command the servomotors based on the positions of these objects measured in real time. A suitable control law is developed for this feedback loop, and is verified by experiments, which demonstrate successful results. The experimental results are compared with those generated by computer simulations under similar conditions.

## I. INTRODUCTION

This paper presents the experimental verification of a novel concept for noncontact magnetic manipulation we proposed in [1]–[3]. This concept was then implemented in [4] as the experimental setup of Fig. 1, which was adopted with minor modifications in this work for its experimental verification. This setup consists of 6 diametrically magnetized permanent magnets actuated by 6 rotary servomotors aimed to control their headings, and thereby, their aggregate magnetic field inside a circular workspace encircled by the magnets. This magnetic field interacts with a small magnetic object inside the workspace to drive it by an applied magnetic force along any desired direction. By feedback control of this magnetic force, the magnetic object is then precisely steered along a desired reference trajectory. A similar concept for magnetic manipulation has been also studied by other researchers [5].

In addition to experimental validation, this paper improves our earlier control design procedures, specially, the optimal linear feedback we developed in [3]. To develop a practical controller for the highly nonlinear dynamics of the proposed magnetic manipulator, we adopted a simple approach in [3] that begins with linearizing the nonlinear dynamics around an, as yet, undecided equilibrium point, then proceeds with the design of a linear controller for the linearized model, and finally ends up with optimizing the control performance with the best choice of the equilibrium point. This paper improves this procedure by including an additional step in which the linear control is modified into a nonlinear control at a higher

This work was supported by the National Science Foundation under Grant No. ECCS-1941944.

The authors are with the School of Electrical, Computer, and Biomedical Engineering, Southern Illinois University, Carbondale, IL, 62901 USA email: {janakamwm, lahiru.ekanayake, akomaee}@siu.edu.

performance. Several experiments under the modified control demonstrate successful steering of a small magnetic bead along reference trajectories in the vicinity of the equilibrium point. We are still working to implement more advanced control techniques such as the feedback linearization in [2].

Our broader efforts to develop new approaches to magnetic manipulation are mainly motivated by potential applications in a range of minimally invasive medical procedures in which external magnetic fields will be leveraged to safely navigate magnetized surgical tools inside the patient's body [6]–[12]. For these applications, relatively strong magnetic forces are required at distances as far as several decimeters, which can be more effectively generated by permanent magnets rather than electromagnets [13], which are the conventional choice for magnetic manipulation [14]–[18]. Hence, our research is dedicated to the class of magnetic manipulators that combine permanent magnets with electromechanical actuators in order to generate and control magnetic fields [1]–[3], [19], [20].

The rest of this paper is organized as follows. In Section II, a short description of the experimental setup is presented and its dynamics is described by a set of nonlinear state-space equations. The procedure for control design and optimization is explained in Section III. Experimental results and their comparison to simulated data are presented in Section IV.

# II. EXPERIMENTAL SETUP AND ITS DYNAMICS

The experimental setup employed in this work is shown in Fig. 1. The magnetic manipulator in this figure consists of a circular flat workspace housing a Petri dish, an array of 6 diametrically magnetized permanent magnets placed at equal distances around the workspace, and a rotary servomotor for each magnet to independently control its direction. The Petri dish is filled with a viscous fluid (corn syrup) and contains a soft magnetic bead moving in a plane at the bottom of the Petri dish under the aggregate magnetic force applied by all 6 magnets. A high-speed camera is fixed above the workspace to measure the real-time position of the magnetic bead as it moves within its plane of motion.

The overall system in Fig. 1 has been designed modularly consisting of several replaceable parts designed separately by SolidWorks and fabricated by 3D printing [4]. The diameter of workspace in this system is 60 mm and the diameter of the Petri dish is currently 39 mm (can be selected up to 60 mm). The magnetic bead is a sphere of 3 mm diameter and 0.11 gm mass made of steel with a magnetic susceptibility of 1000. The permanent magnets in use are grade 42 NdFeB cylinders of diameter and height 19.05 mm, the rotary servomotors are Dynamixel model AX-18A, and the camera is a monochrome



Fig. 1. Experimental setup adopted from [4] with modifications in the size of magnets, design of camera mount, and inclusion of a rigid base structure. This magnetic manipulator (bottom left) utilizes 6 diametrically magnetized cylindrical permanent magnets that can freely rotate a full 360° inside their guiding cylinders using 6 independent servomotors (bottom right).

Allied Vision Mako U-130B with a ON Semi PYTHON 1300 image sensor a resolution of  $1280 \times 1024$  pixels at 169 fps.

The goal of magnetic manipulation in this work is to drive the magnetic bead along reference trajectories confined in a plane at the bottom of the Petri dish. This control task is realized by a feedback loop that measures the position of the magnetic bead in real time, and generates suitable reference signals to the array of servomotors, updated every 90 msec. This control loop is set up by a desktop computer connected to the servomotors at one end and to the camera at another end. This computer runs the real-time software LabVIEW for two purposes: extracting the position of the magnetic bead from images captured by the camera, and incorporating this position into the feedback law of Section III to generate references for the servomotors.

## A. Dynamics of the Magnetic Manipulator

The dynamics of the magnetic manipulator in Fig. 1 was extensively studied in [1]–[3]. This dynamics is described in this paper by a state-space model adopted from [3] with some modifications in the dynamics of the servomotors. The model utilized in this paper includes 16 state variables forming two 2-dimensional vectors r(t) and v(t), and two 6-dimensional vectors  $\theta(t)$  and v(t). Here, v(t) denotes the position of the magnetic bead at time t in a planar coordinate system at the center of the circular workspace. Also,  $v(t) = \dot{r}(t)$  denotes the velocity of the magnetic bead with respect to the same coordinate system. The 6-dimensional vectors v(t) and v(t)0 contain the angular positions (with respect to certain fixed references) and angular velocities of the servomotors.

The control input  $u\left(t\right)$  to the overall magnetic manipulator is a 6-dimensional vector including the reference signals to 6 servomotors, each reference controlling the angular position of its corresponding servomotor. These reference inputs are calibrated in such a manner that  $\theta\left(t\right)$  closely tracks  $u\left(t\right)$  to ideally achieve  $\theta\left(t\right)=u\left(t\right)$ . For a practical servomotor,

this ideal relationship must be modified properly to reflect its actual dynamics. Specifically, the servomotor dynamics in this paper is described by the second-order transfer function

$$H_{\text{servo}}(s) = \frac{\omega_n^2}{s^2 + 2\zeta\omega_n s + \omega_n^2},$$
 (1)

where  $\omega_n$  and  $\zeta$  are positive constants known as the natural frequency and damping ratio of the servomotor, respectively. For the servomotor used in this paper, the numerical values  $\omega_n=75$  rad/sec and  $\zeta=0.75$  have been determined in [19] by experiments, which are identically adopted in this work.

The dynamics of the magnetic manipulator of Fig. 1 is represented by the nonlinear state-space equations

$$\dot{r}\left(t\right) = v\left(t\right) \tag{2a}$$

$$\dot{v}(t) = -\sigma v(t) + g(r(t), \theta(t))$$
 (2b)

$$\dot{\theta}\left(t\right) = \omega\left(t\right) \tag{2c}$$

$$\dot{\omega}(t) = -2\zeta\omega_n\omega(t) - \omega_n^2\theta(t) + \omega_n^2u(t). \tag{2d}$$

Among these equations, (2a) is simply the trivial relationship between the position and velocity of the magnetic bead, while (2c) and (2d) represent the transfer function (1) in the time domain and a vector form. The state equation (2b) is highly nonlinear and is derived from Newton's second law, describing the motion of the magnetic bead under an applied magnetic force and the Stokes drag force acting against the motion as it moves inside a viscous fluid. This equation is examined in more detail next.

The magnetic bead is a sphere of radius  $\rho$  and mass m, and the viscosity of its surrounding fluid is  $\eta$ . The magnetic force is a function  $F_m\left(r,\theta\right)$  of the position r of the magnetic bead and the angular positions  $\theta$  of the permanent magnets. The Stokes drag is known [16] to be  $6\pi\rho\eta v\left(t\right)$ . Newton's second law of motion implies that

$$m\dot{v}(t) = -6\pi\rho\eta v(t) + F_m(r(t),\theta(t)),$$

which can be rewritten as (2b) by defining the vector function

$$g\left(r,\theta\right) = \frac{F_m\left(r,\theta\right)}{m}$$

and the positive parameter  $\sigma=6\pi\rho\eta/m$ . A numerical value of  $\sigma=642.6$  1/sec was determined for this parameter for  $\rho=1.5$  mm, m=0.11 gm, and  $\eta=2.5$  Pa.sec.

The vector function  $g\left(r,\theta\right)$  represents the magnetic force per unit of mass and can be regarded as magnetic acceleration at a point r of the workspace. An explicit expression for this function has been derived in [1]–[3] in terms of the geometry of the magnetic manipulator, the known relationship between magnetic force and magnetic field, and a model of magnetic field for the individual permanent magnets. Throughout this work, this explicit expression was adopted for computation of  $g\left(r,\theta\right)$  or its partial derivatives, whenever necessary. The magnetic field of the individual magnets was constructed by a combination of COMSOL finite element simulations and least squares interpolation techniques.

#### III. CONTROLLER DESIGN

This section develops a simple, yet effective, feedback law for the magnetic manipulator of Fig. 1, which aims to drive small magnetic beads along planar reference trajectories near the center of its workspace. The control design is performed in several steps: linearization of the nonlinear dynamics (2) around an optimally selected equilibrium point, reducing the dimension of the linearized model, design of a linear control for the reduced order linear model, mapping this control back to the original high dimensional state space, and optimizing the control performance in this high dimensional state space.

# A. Linearization and Model Reduction

To facilitate the control design procedure, the nonlinear state-space equations (2) are linearized around an equilibrium point at the center r=0 of the workspace. For any constant vector  $\theta_e$  that holds  $g\left(0,\theta_e\right)=0$ , application of  $u\left(t\right)=\theta_e$  to the state-space equations (2) creates an equilibrium point at  $(r,v,\theta,\omega)=(0,0,\theta_e,0)$ . For the purpose of this paper,  $\theta_e$  is chosen to be a vector with equal elements  $\vartheta$ , i.e.,  $\theta_e=\vartheta \mathbf{1}_6$ , where  $\mathbf{1}_6$  denotes a  $6\times 1$  vector with all elements 1. It is easy to verify that  $g\left(0,\vartheta \mathbf{1}_6\right)=0$  due to the geometric symmetry of the magnetic manipulator around its center.

To linearize the state-space equations (2),  $g(r, \theta)$  in (2b) is approximated by the first two terms of its Taylor series as

$$g(r,\theta) \simeq G_r(0,\theta_e) r + G_\theta(0,\theta_e) (\theta - \theta_e).$$
 (3)

Here,  $G_r\left(0,\theta_e\right)$  and  $G_\theta\left(0,\theta_e\right)$  are  $2\times 2$  and  $2\times 6$  Jacobian matrices of  $g(r,\theta)$  with respect to r and  $\theta$ , respectively. In particular, for  $\theta_e=\vartheta\mathbf{1}_6$ , the Jacobian matrix  $G_r\left(0,\vartheta\mathbf{1}_6\right)$  is diagonal with equal diagonal elements  $a\left(\vartheta\right)$ . For the sake of simplicity, the Jacobian matrix  $G_\theta\left(0,\vartheta\mathbf{1}_6\right)$  is denoted by the  $2\times 6$  matrix  $B\left(\vartheta\right)$ . Then, the linear approximation of the state-space equations (2) around  $(0,0,\vartheta\mathbf{1}_6,0)$  is given by

$$\dot{r}\left(t\right) = v\left(t\right) \tag{4a}$$

$$\dot{v}(t) = -\sigma v(t) + a(\vartheta) r(t) + B(\vartheta) \tilde{\theta}(t)$$
 (4b)

$$\dot{\tilde{\theta}}(t) = \omega(t) \tag{4c}$$

$$\dot{\omega}(t) = -2\zeta\omega_n\omega(t) - \omega_n^2\tilde{\theta}(t) + \omega_n^2\tilde{u}(t), \qquad (4d)$$

where  $\tilde{\theta}(t) = \theta(t) - \vartheta \mathbf{1}_6$  and  $\tilde{u}(t) = u(t) - \vartheta \mathbf{1}_6$  denote the state and control vectors of the linearized model.

The set of linear state-space equations (4) includes 16 state variables, which can be readily reduced to 8 by adopting new state vectors  $\tilde{\theta}_2(t) = B(\vartheta) \tilde{\theta}(t)$  and  $\omega_2(t) = B(\vartheta) \omega(t)$  of the lower dimension 2, and a 2-dimensional control vector

$$z(t) = B(\vartheta) \tilde{u}(t)$$
.

Left multiplying (4c) and (4d) by  $B(\vartheta)$  and using the new vectors  $\tilde{\theta}_2$ ,  $\omega_2$ , and z, the state-space equations (4) reduce to

$$\dot{r}(t) = v(t)$$

$$\dot{v}(t) = -\sigma v(t) + a(\vartheta) r(t) + \tilde{\theta}_2(t)$$

$$\dot{\tilde{\theta}}_2(t) = \omega_2(t)$$

$$\dot{\omega}_2(t) = -2\zeta \omega_n \omega_2(t) - \omega_n^2 \tilde{\theta}_2(t) + \omega_n^2 z(t).$$

This reduced set of equations includes 4 2-dimensional state vectors and all coefficients in their right-hand side appear as scalars, rather than matrices. Hence, the dynamics of the first and the second elements of these vectors are decoupled and can be independently controlled by the first and the second elements of  $z\left(t\right)$ . The relationship between element i=1,2 of  $r\left(t\right)$  and the element i=1,2 of  $z\left(t\right)$  is given by the transfer function

$$H(s) = \frac{1}{s^2 + \sigma s - a(\vartheta)} \cdot \frac{\omega_n^2}{s^2 + 2\zeta\omega_n s + \omega_n^2}.$$
 (5)

#### B. Design of Linear Control

Once the value of  $\vartheta$  is decided, the transfer function (5) is fully known and a linear controller can be readily designed for it. The aim of this controller is to drive a magnetic bead along a planar reference trajectory denoted by  $r_d(t)$ , i.e., the position r(t) of the magnetic bead must closely track  $r_d(t)$ . As a starting point, this paper adopts a simple proportional integral (PI) controller for this purpose, while more advanced controllers that, for instance, combine a state feedback with a state observer will be considered in future work. This PI controller is expressed in a vector form as

$$z(t) = K_P(r_d(t) - r(t)) + K_I \int_0^t (r_d(\tau) - r(\tau)) d\tau$$
 (6)

with scalar parameters  $K_P$  and  $K_I$  determined, for instance, using the root locus method.

For the optimal value  $\vartheta^*=36^\circ$  obtained in Section III-D, the numerical value  $a\left(\vartheta^*\right)=256.9$  1/sec $^2$  was estimated for the parameter  $a\left(\vartheta\right)$  in the transfer function (5). The numeric values of other parameters were taken as  $\sigma=642.6$  1/sec,  $\omega_n=75$  rad/sec, and  $\zeta=0.75$ . Based on these values, two pairs of PI parameters were obtained as  $K_P=1900, K_I=0$  (no integral action) and  $K_P=1600, K_I=4$  1/sec, which were used in the experiments reported in Section IV.

# C. Optimization of Control Effort

After computation of z(t) from (6) or any other linear control law, the control  $\tilde{u}(t)$  of the linearized model (4) can be readily determined as the solution to the system of linear algebraic equations

$$B(\vartheta) \tilde{u}(t) = z(t)$$
.

This system of equations is underdetermined as it includes 2 equations but 6 unknowns. Hence, it admits infinitely many solutions, among which, some are preferred for their higher control performance, which are identified by the optimization procedure explained next.

Noting that  $\tilde{\theta}(t) = \theta(t) - \vartheta \mathbf{1}_6$  is the deviation of  $\theta(t)$  from its equilibrium value  $\vartheta \mathbf{1}_6$ , smaller values of  $\|\tilde{\theta}(t)\|$  render (3) a more accurate approximation, under which the nonlinear dynamics (2) is well described by the linear model (4). On the other hand, small values of  $\|\tilde{\theta}(t)\|$  are typically generated by small values of  $\|\tilde{u}(t)\|$ , which motivates the constrained optimization problem

$$\begin{array}{ll} \text{minimize} & \|\tilde{u}\| \\ \tilde{u} \in [-\pi, \pi]^6 & \\ \text{subject to} & B\left(\vartheta\right) \tilde{u} = z\left(t\right) \end{array} \tag{7}$$

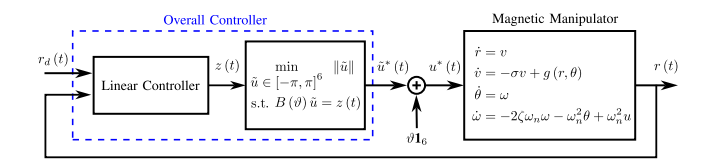


Fig. 2. Block diagram of the closed-loop system under the control (8). The control  $\tilde{u}^*(t)$  is generated in terms of the position r(t) of the magnetic bead and the reference trajectory  $r_d(t)$ .

as a machinery to construct an optimal control  $\|\tilde{u}^*(t)\|$ .

By adopting a 2-norm in this optimization problem, its solution is simply given as the linear control law

$$\tilde{u}^*(t) = B^{\dagger}(\vartheta) z(t), \qquad (8)$$

where  $B^{\dagger}$  is the Moore–Penrose inverse of B defined as

$$B^{\dagger} = B^T \left( B B^T \right)^{-1}$$
.

Under the  $\infty$ -norm, which is a more reasonable choice here, the optimization problem (7) does not have a known closed-form solution. Since numerically solving this problem in real time can be a challenge, an approximate closed-form solution for the problem is presented next.

The core idea of this approximation is to obtain a scalar  $\alpha$  and a vector q of the smallest possible 2-norm such that

$$\tilde{u} = q + \alpha \operatorname{signv} \left( B^{\dagger} \left( \vartheta \right) z \left( t \right) \right)$$

satisfies the constraint  $B\left(\vartheta\right)\tilde{u}=z\left(t\right)$  of (7). Here, signv  $\left(\cdot\right)$  is a vector-valued sign function defined such that

$$\operatorname{signv}(x) = \left[\operatorname{sign}(x_1) \quad \operatorname{sign}(x_2) \quad \cdots \quad \operatorname{sign}(x_n)\right]^T$$

for  $x = \begin{bmatrix} x_1 & x_2 & \cdots & x_n \end{bmatrix}^T$ . Then, the optimal values of  $\alpha$  and q are obtained from the constraint optimization problem

$$\begin{split} & \underset{q \,\in\, \mathbb{R}^{6},\, \alpha \,\in\, \mathbb{R}}{\text{minimize}} & \left\|q\right\|_{2} \\ & \text{subject to} & B\left(\vartheta\right)\left(q + \alpha\operatorname{signv}\left(B^{\dagger}\left(\vartheta\right)z\left(t\right)\right)\right) = z\left(t\right). \end{split}$$

This optimization problem can be analytically solved for

$$\alpha^{*}\left(t\right) = \frac{\|B^{\dagger}\left(\vartheta\right)\left(t\right)\|_{1}}{\|B^{\dagger}\left(\vartheta\right)B\left(\vartheta\right)\operatorname{signv}\left(B^{\dagger}\left(\vartheta\right)z\left(t\right)\right)\|_{2}^{2}}$$
$$q^{*}\left(t\right) = -B^{\dagger}\left(\vartheta\right)\left(\alpha^{*}\left(t\right)B\left(\vartheta\right)\operatorname{signv}\left(B^{\dagger}\left(\vartheta\right)z\left(t\right)\right) - z\left(t\right)\right)$$

that leads to the nonlinear control law

$$\tilde{u}^*(t) = q^*(t) + \alpha^*(t)\operatorname{signv}\left(B^{\dagger}(\vartheta)z(t)\right). \tag{9}$$

The block diagram of Fig. 2 explains how this control law is implemented to establish a feedback loop.

## D. Optimization of Equilibrium Point

The control laws (8) and (9) are both parameterized by  $\vartheta$  and their performance depends on this scalar parameter. This parameter is optimized for the best control performance, following a procedure proposed in [3]. Here, the performance measure is the norm  $\|\tilde{u}(t)\|$  of the control vector, which must be minimized in some reasonable sense. Certainly,  $\|\tilde{u}(t)\|$  is a function of time and cannot be minimized directly to

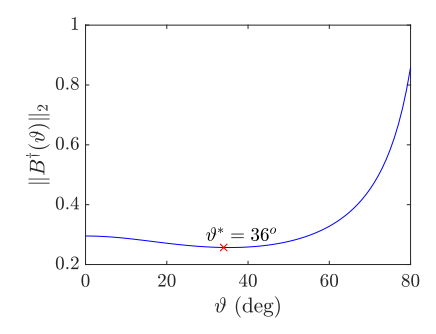


Fig. 3. Optimal value of  $\vartheta$  for selecting the best equilibrium point. The optimization process is performed according to (10) with induced 2-norm of the matrix  $B^{\dagger}(\vartheta)$ .

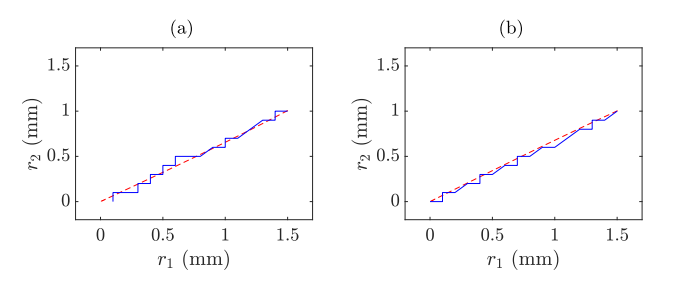


Fig. 4. Trajectory of magnetic bead starting at  $r\left(0\right)=\left(1.5,1\right)$  in its plane of motion and moving toward  $\left(0,0\right)$  under  $r_{d}\left(t\right)=0$  applied to (a) the linear control law (8), and (b) the nonlinear control law (9). The solid and dashed lines represent the results of experiment and simulation, respectively.

obtain a constant  $\vartheta^*$ . Thus, a new performance measure, not depending on time, must be adopted in such a manner that its small values imply small values of  $\|\tilde{u}(t)\|$  for most instances of t. This goal can be achieved via a minimax formulation.

In particular, for the linear control law (8), this minimax problem is given by

$$\begin{array}{ll} \text{minimize} & \text{maximize} \\ \vartheta \in \left[0, \pi/2\right] & \left\|z\right\| = 1 \end{array} \left\|B^{\dagger}\left(\vartheta\right)z\right\|,$$

which is reduced to

$$\underset{\vartheta \in [0, \pi/2]}{\text{minimize}} \quad \|B^{\dagger}(\vartheta)\| \tag{10}$$

in terms of the induced matrix norm  $\|B^{\dagger}(\vartheta)\|$ . In Fig. 3, this optimization problem is solved numerically for induced 2-norm. A similar process can be formulated for the nonlinear control law (9), albeit at a higher computational cost.

# IV. EXPERIMENT AND SIMULATION RESULTS

We conducted a series of experiments on the setup of Fig. 1 under both the linear control law (8) and its nonlinear counterpart (9). Each experiment was paired with computer simulations under similar conditions to examine the possible mismatch between the real-world setup and its mathematical model. The results of this study are presented in this section.

In the first experiment, a magnetic bead was driven from an initial position r(0) = (1.5,1) mm toward (0,0) under the constant reference signal  $r_d(t) = 0$ . This experiment was performed under a pure proportional control  $(K_I = 0)$  with the gain  $K_p = 1900$ . For this experiment, the trajectory of

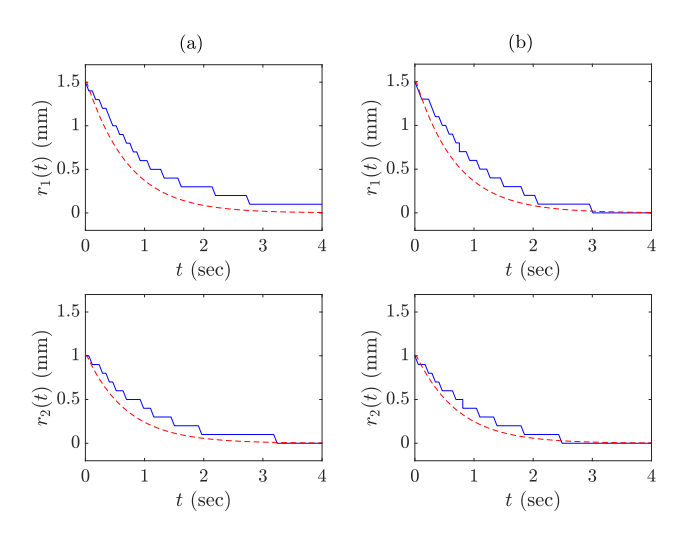


Fig. 5. Position of the magnetic bead versus time generated by experiment (solid line) and simulation (dashed line) under (a) the linear control law (8), and (b) the nonlinear control law (9). The control goal is to drive the magnetic bead from r(0) = (1.5, 1) to (0, 0) by setting  $r_d(t) = 0$ .

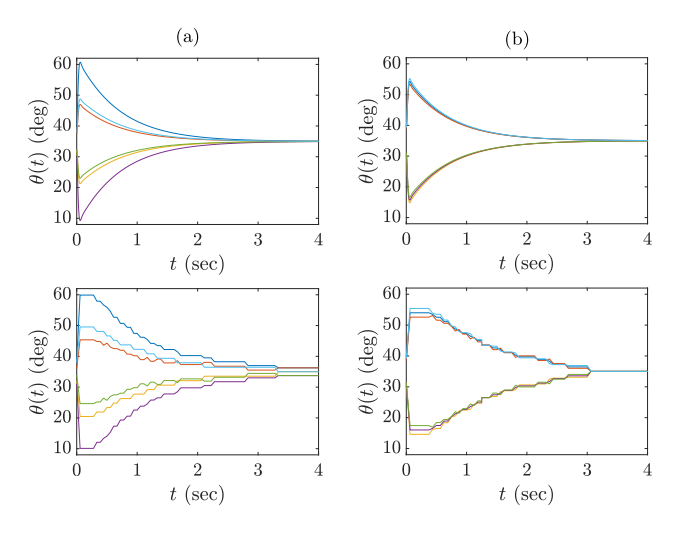


Fig. 6. Servomotor positions versus time generated by simulation (top) and by experiment (bottom) under (a) the linear control law (8), and (b) the nonlinear control law (9). The control goal is similar to Fig. 5.

magnetic bead in its plane of motion is illustrated in Fig. 4, the position of magnetic bead versus time in Fig. 5, and the angular positions of the servomotors versus time in Fig. 6.

Throughout the experiment, the magnetic bead was driven toward the center r=0 of the workspace with an average velocity of 0.52 mm/sec under the linear control law (8) and 0.60 mm/sec under the nonlinear control law (9). These numbers predict a settling time of 3.5 sec for the former and 3.0 sec for the latter. The settling time was estimated by computer simulations around 4.0 sec, which considerably differs from its experimental value. The most likely cause of this difference is a mismatch between the numerical value of viscosity (of corn syrup) in experiment and simulations.

The performance of trajectory tracking under both control laws (8) and (9) was evaluated in the second experiment. To that end, a slowly-varying reference  $r_d\left(t\right)$  was applied to the

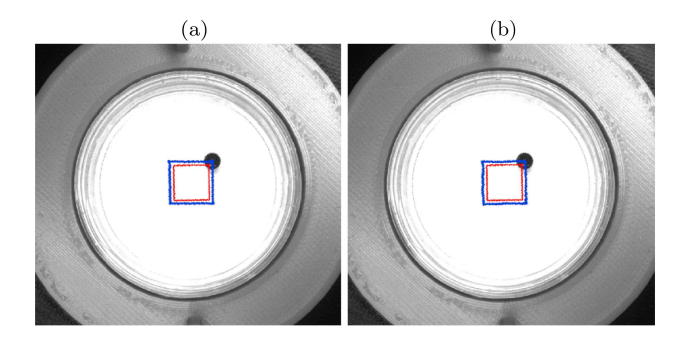


Fig. 7. Trajectory of the magnetic bead (blue line) near a square reference trajectory (red line) with a side length of 6 mm, generated under (a) the linear control law (8), and (b) the nonlinear control law (9).

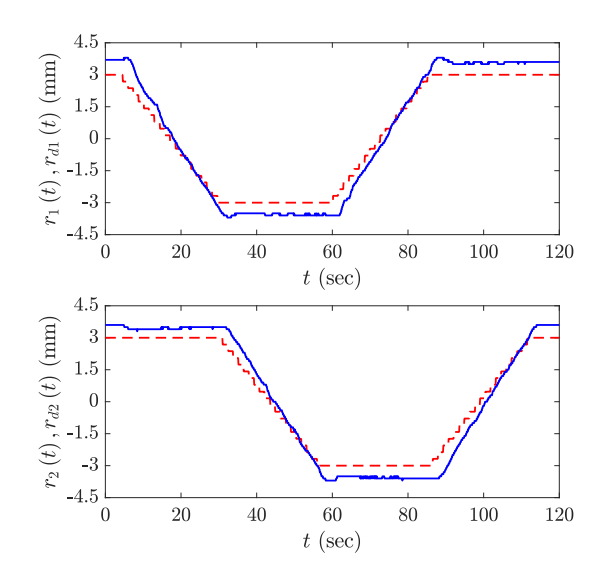


Fig. 8. Position of magnetic bead (solid line) and the reference trajectory (dashed line) in the experiment of Fig. 7 versus time, generated under the linear control law (8).

closed-loop system to create a series of reference trajectories, from simple to more complex. For instance, a square of 6 mm side length is considered as the reference trajectory in Fig. 7. For this reference trajectory, the position  $r\left(t\right)$  of the magnetic bead and the reference input  $r_d\left(t\right)$  are also illustrated versus time in Fig. 8. The performance of trajectory tracking under more complex references is presented in Fig. 9. It is observed from Figs. 7 through 9 that the proportional control utilized in the experiments overall is capable of steering a magnetic bead along complex trajectories, albeit with a significant tracking error. The average tracking error under this control was estimated around 25%.

To compensate for the relatively large tracking error under the proportional control, a PI controller was adopted with the parameter values  $K_P=1600$  and  $K_I=4$ . The average tracking error for this control was computed at much lower level of only 3%. This error is at the level of measurement error due to the finite resolution of camera, and most likely, is not caused by the control algorithm. Fig. 10 illustrates the performance of the PI controller in tracking a spiral reference trajectory. The travel time of the magnetic bead along this

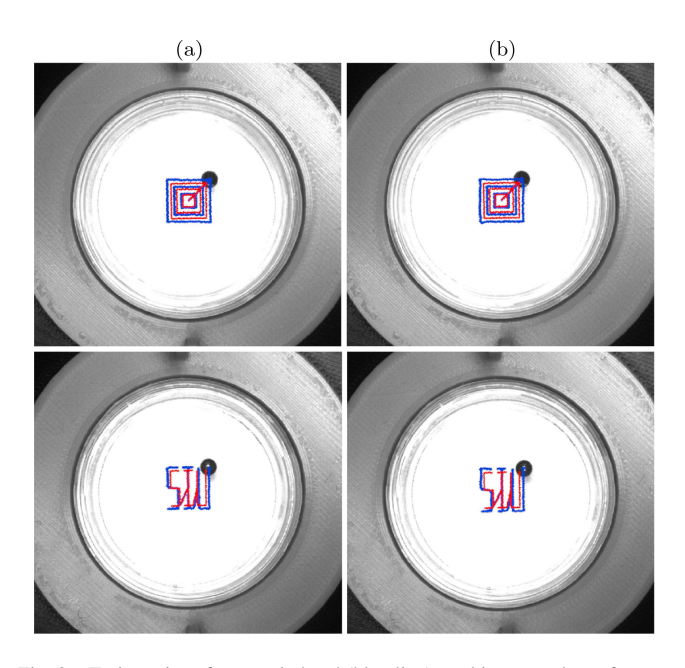


Fig. 9. Trajectories of magnetic bead (blue line) tracking complex reference trajectories (red line) under (a) the linear control law (8), and (b) the nonlinear control law (9). The reference trajectory on top consists of three squares with side lengths of 2 mm, 4 mm, and 6 mm. The SIU-shaped trajectory (bottom) fits within a square of 6 mm side length.

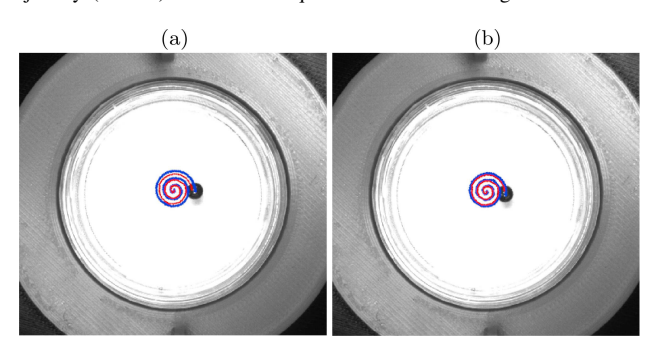


Fig. 10. Comparison between (a) pure proportional and (b) PI controllers embedded into the linear control law (8). The proportional control results in a larger tracking error but is capable of driving the magnetic bead faster. In particular, the travel time under the proportional control is 106 sec versus 295 sec for the PI control. In this figure, the blue and red lines represent the position of the magnetic bead and the reference trajectory, respectively.

trajectory was recorded as 106 sec under proportional control and 295 sec under PI control. These numbers indicate 2.7 times reduction in the speed of the magnetic bead, which is the price paid for a lower tracking error.

# V. CONCLUSION

The major results of this work are twofold. First, the early concept of magnetic manipulation using permanent magnets and electromechanical actuators was realized and validated by experiments. The success in these experiments motivates further research efforts on this concept, which eventually can yield a framework for design and development of magnetic manipulators suited for a range of medical applications. As the second major result, a procedure for design of feedback control laws was developed, which can be adopted, or at least modified, for magnetic manipulators of different geometries.

## REFERENCES

- [1] N. Riahi and A. Komaee, "Steering magnetic particles by feedback control of permanent magnet manipulators," in *Proc. of 2019 American Control Conference (ACC 2019)*, pp. 5432–5437, 2019.
- [2] N. Riahi, L. R. Tituaña, and A. Komaee, "Homotopy continuation for feedback linearization of noncontact magnetic manipulators," in *Proc.* of 2020 American Control Conference (ACC 2020), pp. 4295–4300, 2020.
- [3] N. Riahi and A. Komaee, "Noncontact steering of magnetic objects by optimal linear feedback control of permanent magnet manipulators," in Proc. of 2020 IEEE/ASME International Conference on Advanced Intelligent Mechatronics (AIM 2020), pp. 30–35, 2020.
- [4] L. R. Tituaña, "Implementation of a planar magnetic manipulator with rotatable permanent magnets," Master's thesis, Southern Illinois University, Carbondale, 2020.
- [5] P. Ryan and E. Diller, "Magnetic actuation for full dexterity microrobotic control using rotating permanent magnets," *IEEE Trans. Robot.*, vol. 33, no. 6, pp. 1398–1409, 2017.
- [6] M. Sendoh, K. Ishiyama, and K.-I. Arai, "Fabrication of magnetic actuator for use in a capsule endoscope," *IEEE Trans. Magn.*, vol. 39, no. 5, pp. 3232–3234, 2003.
- [7] G. Ciuti, P. Valdastri, A. Menciassi, and P. Dario, "Robotic magnetic steering and locomotion of capsule endoscope for diagnostic and surgical endoluminal procedures," *Robotica*, vol. 28, no. 2, pp. 199– 207, 2010.
- [8] M. Simi, P. Valdastri, C. Quaglia, A. Menciassi, and P. Dario, "Design, fabrication, and testing of a capsule with hybrid locomotion for gastrointestinal tract exploration," *IEEE/ASME Trans. Mechatronics*, vol. 15, no. 2, pp. 170–180, 2010.
- [9] S. Yim and M. Sitti, "Design and rolling locomotion of a magnetically actuated soft capsule endoscope," *IEEE Trans. Robot.*, vol. 28, no. 1, pp. 183–194, 2012.
- [10] M. Beccani, C. Di Natali, L. J. Sliker, J. A. Schoen, M. E. Rentschler, and P. Valdastri, "Wireless tissue palpation for intraoperative detection of lumps in the soft tissue," *IEEE Trans. Biomed. Eng.*, vol. 61, no. 2, pp. 353–361, 2014.
- [11] V. Iacovacci, L. Ricotti, P. Dario, and A. Menciassi, "Design and development of a mechatronic system for noninvasive refilling of implantable artificial pancreas," *IEEE/ASME Trans. Mechatronics*, vol. 20, no. 3, pp. 1160–1169, 2015.
- [12] L. Sliker, G. Ciuti, M. Rentschler, and A. Menciassi, "Magnetically driven medical devices: a review," *Expert Review of Medical Devices*, vol. 12, no. 6, pp. 737–752, 2015.
- [13] O. Baun and P. Blümler, "Permanent magnet system to guide superparamagnetic particles," *J MAGN MAGN MATER*, vol. 439, pp. 294– 304, 2017.
- [14] E. G. Quate, K. G. Wika, M. A. Lawson, G. T. Gillies, R. C. Ritter, M. S. Grady, and M. A. Howard, "Goniometric motion controller for the superconducting coil in a magnetic Stereotaxis system," *IEEE Trans. Biomed. Eng.*, vol. 38, no. 9, pp. 899–905, 1991.
- [15] M. P. Kummer, J. J. Abbott, B. E. Kratochvil, R. Borer, A. Sengul, and B. J. Nelson, "OctoMag: An electromagnetic system for 5-DOF wireless micromanipulation," *IEEE Trans. Robot.*, vol. 26, no. 6, pp. 1006–1017, 2010.
- [16] R. Probst, J. Lin, A. Komaee, A. Nacev, Z. Cummins, and B. Shapiro, "Planar steering of a single ferrofluid drop by optimal minimum power dynamic feedback control of four electromagnets at a distance," J MAGN MAGN MATER, vol. 323, no. 7, pp. 885–896, 2011.
- [17] A. Komaee and B. Shapiro, "Steering a ferromagnetic particle by optimal magnetic feedback control," *IEEE Trans. Control Syst. Technol.*, vol. 20, no. 4, pp. 1011–1024, 2012.
- [18] S. Afshar, M. B. Khamesee, and A. Khajepour, "Optimal configuration for electromagnets and coils in magnetic actuators," *IEEE Trans. Magn.*, vol. 49, no. 4, pp. 1372–1381, 2013.
- [19] M. Mohammadzadeh, M. R. Shariatmadari, N. Riahi, and A. Komaee, "Feedback decoupling of magnetically coupled actuators," in Proc. of the 2021 IEEE/ASME International Conference on Advanced Intelligent Mechatronics (AIM 2021), pp. 320–325, 2021.
- [20] M. R. Shariatmadari and A. Komaee, "Feedback stabilization of a permanent magnet levitation system," in *Proc. of the 2022 American Control Conference (ACC 2022)*, pp. 5087–5092, 2022.